ELSEVIER

Polymer 44 (2003) 821–840

polymer

www.elsevier.com/locate/polymer

A new 'Tailor-made' methodology for the mechanical behaviour analysis of rubber-like materials: II. Application to the hyperelastic behaviour characterization of a carbon-black filled natural rubber vulcanizate

Fazilay Laraba-Abbes[a,*], Patrick Ienny[b,1], Roland Piques[c,2]

[a]*Centre des Matériaux P.M. Fourt, Ecole des Mines de Paris, BP 87, F91003 Evry Cedex, France*
[b]*Centre des Matériaux de Grande Diffusion, Ecole des Mines d'Alès, F30390 Alès Cedex, France*
[c]*Centre des Matériaux P.M. Fourt, Ecole des Mines de Paris, BP 87, F91003 Evry Cedex, France*

Received 3 March 2002; received in revised form 1 September 2002; accepted 4 September 2002

Abstract

The purpose of this paper is the modelling of the mechanical behaviour of an elastomeric material, through detailed experimental and numerical procedures, specific to large strains. The experimental technique is based on in-plane kinematics measurements using a speckle extensometer, from which the whole two-dimensional field of in-plane displacements is obtained by a digital image processing [Polymer (2002)]. This part of the work concerns the identification of the constitutive equation for a carbon black natural rubber (NR) vulcanizate. We start by quoting some theoretical considerations relative to rubber elasticity and stress-softening effect, which is the counterpart of the filler reinforcement. Then, we describe the experimental procedure and present data for both non-preconditioned and preconditioned samples. Next, the identification of the constitutive law parameters using a minimization algorithm is driven. Finally, we present the validation of the constitutive model, by its implementation into the finite element code SYSTUS and the numerical simulation of the response of a double edge notched tensile (DENT) specimen.

Keywords: Natural rubber; Hyperelastic constitutive law; Mullins' effect

1. Introduction

Natural and synthetic rubbers exhibit such a number of physical and chemical properties that they form a large family of materials able to meet a wide range of requirements. Obviously, their numerous domains of use result not only from their vulcanization but also, above all, from the addition of active fillers such as carbon black or silica. This incorporation is of significant commercial importance due to the enhancement of both mechanical and physical properties of the final materials.

The behaviour of elastomeric materials is complex, including very high deformability, quasi—incompressibility, stress-softening effect (also called Mullins effect) and time-dependent effects. Hence a correct description of their behaviour must include both geometric and material non-linearities.

We propose a new methodology for the mechanical behaviour analysis of rubber-like materials, within the framework of finite transformations, from the kinematics measurements of two-dimensional in-plane displacements associated to homogeneous and non-homogeneous deformation modes, to the identification and the validation of the constitutive equation.

The experimental technique used here, based on the laser speckle effect, has been described and calibrated in the first part of this work [1]. The digital speckle extensometry presents several points of interest. It gives access to a two-dimensional field of in-plane displacements by a digital image processing, with a high spatial resolution (about 10 μm/pixel). Furthermore, it is non-contact, non-intrusive and it requires no preparation of the sample.

The present paper is devoted to the hyperelastic behaviour analysis of a carbon black (CB) filled natural

* Corresponding author. Address: 5 Boulevard Franchet, d'esperery, Reims 51100, France. Tel.: +333-26-50-24-75.
E-mail addresses: fazilay_abbes@hotmail.com (F. Laraba-Abbes), patrick.ienny@ema.fr (P. Ienny), roland.piques@mat.ensmp.fr (R. Piques).
[1] Tel.: +334-66-78-56-32; fax: +334-66-78-56-80.
[2] Tel.: +331-60-76-30-52; fax: +331-60-76-31-60.

0032-3861/03/$ - see front matter © 2002 Elsevier Science Ltd. All rights reserved.
PII: S0032-3861(02)00719-X

rubber (NR) vulcanizate. Section 2 presents some elements of rubber elasticity and the most commonly-used forms for the elastic energy density per unit volume of unstrained body, belonging either to the micromechanical approach or to the phenomenological one. The damage-induced phenomenon is also treated from the two points of view. We end this section with the constitutive equation and the model parameters to identify. In Section 3 the experimental procedure is briefly described, and two-dimensional data issued from uniaxial traction (UT) and pure shear (PS) tests on both non-preconditioned and preconditioned material are presented. We have also conducted non-homogeneous mechanical tests on non-preconditioned material, for the validation of the constitutive equation. Section 4 presents the optimization procedure, and the numerical results relative to the identification of the material parameters from the homogeneous experimental tests. Section 5 is devoted to the implementation procedure of our constitutive law into the finite element code SYSTUS, and to the validation of the model by comparison between the experimental non-homogeneous tensile response of a double edge notched tensile (DENT) specimen and its numerical one issued from a finite element analysis (FEA) simulation. Finally some conclusions are drawn.

2. Theoretical considerations

2.1. The rubber elasticity

The continuum mechanical derivation of constitutive equations for elastomeric compounds is based on the concept of a strain energy density function or elastic potential W, corresponding to the change in the Helmholtz free energy of the material upon deformation. It is supposed throughout that the material is isotropic and homogeneous, and that the temperature remains constant. In the literature relating to rubber elasticity, one can find many theoretical models. The most commonly-used ones are reviewed hereafter.

Two approaches are generally considered for the rubber isothermal mechanical behaviour characterization: the kinetic theory which is based on statistical thermodynamics considerations, and the phenomenological approach which treats the material as a continuum regardless of its microstructural and molecular nature.

2.1.1. The kinetic theory

This approach dates back to the 1940s. It attempts to derive elastic properties from some idealized model of the structure of vulcanized rubber. This theory, which is one of the cornerstones of our understanding of the macromolecular nature of rubber, is based on observations that the rubber elastic deformation arises almost entirely from the decrease in entropy with increase in the applied extension. It generally deals with assumed statistical distributions of the lengths, orientations and structure of rubber molecular networks. Investigators have built networks from chains described by Gaussian statistics, that is the chains never approach their fully extended length, or have modified the chain statistics to allow larger stretches than are afforded by the Gaussian chain, then incorporated these non-Gaussian chains into networks of three, four or eight number of chains. For instance, one can mention the Gaussian network [2–4], the phantom chain [5,6], and the Langevin chain [7]. More recently, Boyce and Arruda [8] proposed a fully three-dimensional model, in which eight orientations of chains in space give rise to the well-known eight-chain-network.

2.1.2. The phenomenological approach

Following Rivlin [9], this approach starts with the basic assumptions that the material is isotropic and its isothermal elastic properties may be described in terms of a strain energy function W. Numerous strain energy density functions have been proposed, and can be subdivided according to whether W is expressed as a polynomial function of strain invariants, or directly in terms of principal stretch ratios, and whether incompressibility is assumed or not [10].

(a) Strain invariant based models. Rivlin [9] has pointed out that the strain energy density function W can be approximated by the power series:

$$W = \sum_{i+j+k=1}^{\infty} c_{ijk}(I_1 - 3)^i(I_2 - 3)^j(I_3 - 3)^k \tag{1}$$

where c_{ijk} denote the material constants and I_1, I_2 and I_3 are the strain invariants, given by:

$$I_1 = \lambda_1^2 + \lambda_2^2 + \lambda_3^2$$
$$I_2 = (\lambda_1\lambda_2)^2 + (\lambda_2\lambda_3)^2 + (\lambda_3\lambda_1)^2 \qquad I_3 = (\lambda_1\lambda_2\lambda_3)^2 \tag{2}$$

where $\lambda_1, \lambda_2, \lambda_3$ refer to the three principal extension ratios (also called principal stretches). Notice that a principal extension ratio is defined as the ratio of the final length to the initial one in the direction of the corresponding principal strain axis (subscripts 1–3 denote three mutually orthogonal directions).

The quantities $(I_1 - 3)$, $(I_2 - 3)$ and $(I_3 - 3)$ are used rather than I_1, I_2 and I_3 in order that the strain energy density function be conventionally taken as zero in the unstrained state. The parameter c_{000} is taken as zero for the same reason.

The third strain invariant I_3 can be interpreted in physical terms as the square of the ratio between the volumes of a material element in the deformed and undeformed states. It follows that for incompressible materials $\lambda_1\lambda_2\lambda_3 = 1$ and therefore $I_3 = 1$. Eq. (2) may be written solely in terms of, say, λ_1 and λ_2 (with $\lambda_3 = 1/\lambda_1\lambda_2$):

$$I_1 = \lambda_1^2 + \lambda_2^2 + \frac{1}{\lambda_1^2\lambda_2^2} \qquad I_2 = \lambda_1^2\lambda_2^2 + \frac{1}{\lambda_1^2} + \frac{1}{\lambda_2^2} \tag{3}$$

and Eq. (1) reduces to the well-known Rivlin-type strain-energy density function:

$$W = \sum_{i+j=1}^{\infty} c_{ij}(I_1 - 3)^i (I_2 - 3)^j \tag{4}$$

The power series in Eq. (4) is usually truncated by taking only the leading terms. Retaining only the first term yields the neo-Hookean model:

$$W = c_{10}(I_1 - 3) \tag{5}$$

and an expansion using two terms as in the work of Mooney [11] leads to the commonly-known Mooney–Rivlin form:

$$W = c_{10}(I_1 - 3) + c_{01}(I_2 - 3) \tag{6}$$

While the Mooney–Rivlin equation is convenient for its simplicity, it is often found to be inadequate for predicting stress–strain curves for multiaxial deformation modes, especially at high strain levels. Tschoegl [12] suggests that the failure of the Mooney–Rivlin form to provide adequate multiaxial data predictions arises from not taking enough terms in the expansion of Eq. (4).

Thus, several expressions of the strain energy density function involving higher order terms have been proposed. One can mention the so-called third-order deformation approximation [13,14]:

$$W = c_{10}(I_1 - 3) + c_{01}(I_2 - 3) + c_{11}(I_1 - 3)(I_2 - 3) + c_{20}(I_1 - 3)^2 + c_{30}(I_1 - 3)^3 \tag{7}$$

(b) Stretch ratio based models. The second major class of strain-energy density functions are those based on polynomials of the principal extension ratios λ_1, λ_2 and λ_3.

The most popular strain potential belonging to this category is the well-known strain-energy density function of Ogden [15]. This model is implemented in numerous commercial finite element packages and is frequently used as a benchmark in rubber elasticity. For an incompressible material, its expression follows:

$$W = \sum_{i=1}^{n} \frac{2\mu_i}{\alpha_i^2}(\lambda_1^{\alpha_i} + \lambda_2^{\alpha_i} + \lambda_3^{\alpha_i}) \tag{8}$$

where μ_i and α_i are arbitrary constants determined from experimental data. The exponent values α_i can be any real number which gives the ability to fit quite non-linear data. To ensure physically reasonable responses, the strain energy density function must satisfy certain restrictions. In practice, in respect of a certain constitutive inequality due to Hill [16,17], the conditions:

$$\mu_i \alpha_i \geq 0 \quad \text{(each } i\text{; no summation)} \tag{9}$$

are sufficient. When the strain-energy density function comprises either one or two (α,μ) terms only, these conditions are also necessary [15]. When there are three or more (α,μ) terms, not all the conditions (9) are necessary.

It is implicit in all such functions that rubber behaves as perfectly elastic material although it is well known that filled rubbers especially exhibit significant departures from elasticity such as hysteresis, stress-softening and permanent set. We introduce hereafter some elements relative to the (strain-induced) stress-softening phenomenon, experimentally observed while testing our material. We must obviously take this effect into account for an efficient and realistic description of the mechanical behaviour of our material.

2.2. The stress-softening or Mullins effect

Cyclic loading of filled elastomers shows non-linear elastic and inelastic material characteristics. The latter properties yield hysteresis loops which stand for the dissipated energy per cycle of deformation. Dependent on the history of straining, e.g. the extent of previous stretching, the rubber material undergoes an almost permanent change that alters the elastic properties and increases hysteresis. The strong reduction of the stiffness found at first loading is referred to as the 'Mullins effect'. Most of the softening occurs in the first deformation and after a few deformation cycles the rubber approaches a steady state with a constant stress–strain behaviour. Furthermore, the softening is usually only present at deformations smaller than the previous maximum.

Stress-softening has been the subject of many experimental [18–23] and theoretical investigations, and several mechanisms responsible for the phenomenon have been proposed. No theoretical explanation was forthcoming from these early investigations and it was 1947 before work carried out by Mullins [24,25] was sufficiently quantitative for theoretical considerations to be attempted. These experimental contributions led to the description of the phenomenon of stress-softening in filler loaded rubbers as the Mullins effect.

2.2.1. Stress-softening mechanisms

The mechanical behaviour of filler-reinforced vulcanized rubbers depends primarily on extremely complex associations being formed during the fabrication process. A so-called primary (or chemical) bonding of molecular chains is merely attributed to vulcanization and polymerization. This chemical bonding process, primarily activated near the processing temperature, becomes inactivated or slowed-down after the cooling down stage. Further a secondary (or physical) bonding is thought to be due to formation of entanglements, and of rubber–filler and filler–filler attachments. It is assumed that the relatively weak secondary bonding may rupture or slip due to the application of relatively small external loading, giving rise to the rubber hysteresis and stress-softening behaviour in cyclic loading situations.

Molecular slippage mechanisms as a source of energy loss and stress-softening have been proposed many times.

Bueche [26], Dannenberg [27] and Boonstra [28] attributed stress-softening primarily to the successive breakage of network chains between adjacent filler particles, without distinction between the break occurring at the filler surface or along the chain itself. The detachment or breakage of the chains occurred when the filler particles separated sufficiently to stretch the shortest molecular chains to their full extension.

2.2.2. Damage models incorporating the Mullins effect

The expression 'damage' is ambiguous in the field of mechanics. In fracture mechanics it describes macro cracks and delaminations. However, in this paper damage is understood as a reduction of the material's stiffness as a result of micro defects like chain and multichain damage, microstructure damage and microvoid formation (cavitation).

A lot of different models have been proposed, some of them involving micromechanical concepts, and other based on a phenomenological approach.

(a) The microscopic approach. From the micromechanical viewpoint, Mullins and Tobin [29] proposed a model which considers the stress-softening material as a two-phase system consisting of a hard phase and a soft phase. They reasoned that initially the rubber existed solely in the hard phase and that as it was subjected to greater and greater deformation more and more of the rubber would degrade into the soft phase. Although one may think of the soft phase as the pure gum, and the hard phase as the filler, the model is not so restrictive. The conversion of the hard phase to the soft phase is measured through a damage parameter, which the authors related to strain amplification in the remaining hard phase of the rubber. Furthermore, the notion of 'strain amplification factor' has been used by Bueche [26,30], Harwood et al. [31], Harwood and Payne [32,33] and more recently Johnson and Beatty [34,35], among others. Govindjee and Simo [36] proposed a fairly complex hyperelastic-based damage model, within the scope of an averaging-theory and using tools issued from statistical mechanics. Considering a statistically representative sample volume (SRSV), the model consists of an overall free energy density function for the composite system constructed in terms of the constituent free energies. The filler particles have been assumed rigid, so that the average macroscopic strain of the SRSV has been related to the average strain in the matrix material. In practice, the evaluation of the free energy for the rubber vulcanizate involves the probabilities under given average strain levels for different polymer network configurations. Within this framework, the mean free energy is given as a sum over all possible configurations of the configurational probability times the free energy of the configuration. Damage fits into this notion by changing the configurational probabilities and/or the free energies of the configurations.

(b) The macroscopic approach. The phenomenological modelling of softening materials using continuum damage mechanics goes back to Lemaître [37], Kachanov [38], and Chaboche [39], among others. Govindjee and Simo [40] proposed a transition from micro-mechanics to a computationally efficient phenomenological model incorporating Mullins effect. In particular, the damage evolution is governed by the maximum stretch of the deformation history.

Nevertheless, experimental investigations of filled elastomers indicate that a damage accumulation also occurs for strain cycles which have values of effective free energy below the maximum value of the past history. Miehe [41] has accounted for this phenomenon by adding to the discontinuous damage observed during the first cycle of a loading process a continuous damage cumulated within the whole strain history of the deformation process. Following Miehe, the change in free energy, W, within an isothermal elastic deformation from the reference configuration to the current configuration is given by:

$$W = (1 - d)W_0 \tag{10}$$

where W_0 refers to an effective strain energy density function with respect to the undamaged material, and $d \in [0,1]$ is a scalar internal variable which describes an isotropic damage effect, that is the elastic softening of the material. This isotropic scalar model is usually employed for rubber material although some anisotropic features are found.

The total damage variable d is described by the following constitutive equation:

$$d = d_\alpha(\alpha) + d_\beta(\beta) \tag{11}$$

d_α is related to the so-called discontinuous damage occurring only within the first cycle of a deformation process. Further strain cycles below a maximum effective strain energy do not contribute to this kind of damage. Independently of the mechanism above, a continuous damage accumulation within the whole strain history of the deformation process is taken into account through the scalar damage variable d_β.

The discontinuous damage is assumed to be governed by the variable:

$$\alpha(t) = \underset{s\in[0,t]}{\text{Max}}\, W_0(s) \tag{12}$$

thus α is simply the maximum thermodynamic force or effective strain energy W_0 of the undamaged material which has been achieved within the history interval $[0,t]$.

The continuous damage is assumed to be governed by the integral:

$$\beta(t) = \int_0^t |\dot{W}_0(s)|\mathrm{d}s \tag{13}$$

Eq. (13) formulates the evolution of softening as function of the change of strain energy (through the time derivative $\dot{W}_0$ of the strain density energy W_0). Thus, it gives a continuous increase in damage even for unloading. In our case, we assumed no increase in damage while unloading the

Table 1
The CB filled NR vulcanizate formulation

Formulation	
Ingredient	Phr
Pure gum	100.0
Zinc oxide	15.0
Stearic acid	1.0
N-772 carbon black	20.0
N-330 carbon black	3.0
Sulphur	≤2.0
Plasticizers	5.0
Accelerators	1.5
Antioxidant	1.5

specimen. This leads to the following modification of the continuous damage formulation:

$$\beta(t) = \int_0^t \langle \dot{W}_0(s) \rangle \mathrm{d}s \tag{14}$$

Finally, the damage functions $d_\alpha(\alpha)$ and $d_\beta(\beta)$ need to be specified in order to define the damage evolution. In Miehe [41], a simple exponential expression with a saturation form is employed. This model is convenient for qualitative studies and yields a symmetric tangent matrix. The saturation form is namely:

$$\begin{cases} d_\alpha(\alpha) = d_\alpha^\infty \left[1 - \exp\left(-\dfrac{\alpha}{\eta_\alpha} \right) \right] \\ \textit{and} \\ d_\beta(\beta) = d_\beta^\infty \left[1 - \exp\left(-\dfrac{\beta}{\eta_\beta} \right) \right] \end{cases} \tag{15}$$

where d_α^∞ and d_β^∞ describe the maximum possible damage of the two damage mechanisms under consideration, satisfying $d_\alpha^\infty + d_\beta^\infty \in [0, 1]$, and η_α and η_β characterize the saturation properties.

3. Experimental procedure and results

We describe here the experimental procedure adopted for the characterization of the mechanical behaviour of an elastomeric material. Homogeneous tests have been carried out to evidence the main characteristics of the response of the material, and to provide the relevant and the pertinent experimental database for the identification of the constitutive equation. Inhomogeneous tests have also been carried out for the validation of the constitutive law. The latter is based on the comparison between the experimental and the numerical responses of a DENT sample, especially the evolution of the strain gradient between the notches of the structure, evidenced by the measure of the strain profiles along the width of the specimen.

3.1. The material under study

The elastomer used throughout this work is a vulcanized CB filled NR vulcanizate. It is obtained by calandering and is conditioned in thin flexible rectangular sheets of 2 mm thickness, which makes the contactless and non-intrusive digital speckle extensometer particularly convenient. The formulation of this compound is given in Table 1.

The filler concentration is approximately 23 phr (parts of Carbon Black per hundred parts of gum). Notice that two CB grades have been incorporated into this vulcanizate's formulation. Used in the automotive industry (silent blocks), the compound has to satisfy optimal reinforcement and dissipation requirements. Moreover, this material has to exhibit a low self-heating and a good fatigue-life-time under dynamic loadings. The main characteristics of this elastomer are listed in Table 2. They correspond to a rubbery behaviour at room temperature. The material is also quasi-incompressible and moderately soft.

3.2. The experimental procedure

The test apparatus uses a DARTEC servohydraulic testing machine, with a 1 kN load cell and pneumatic grips. An Argon (Ar +) laser emitting at the wavelength $\lambda = 514.5$ nm is the light source. An optical apparatus, including diaphragms and lenses, ensures the expansion and the collimation of the laser beam, thus the maximum spot size and power, and the most uniform light intensity illuminating the sample.

High resolution images are recorded at successive states of the deformation via a high resolution CCD camera (KODAK MEGAPLUS 1.4, (1317×1035) squared and joined pixels), set in front of the specimen. The CCD camera is fixed on a motor-driven-micro-displacement stage. This allows the camera to follow the same region under study while the lower clamps are moving. The lens axis of the camera is kept perpendicular to the surface of the sample. Its subsequent displacement during the mechanical test, synchronized to the mid-specimen point displacement, is also kept parallel to the clamps moving direction, by a previous adjustment.

The images are digitized in 1024×1024 pixels. Each pixel represents the intensity of light arriving on the small

Table 2
The CB filled NR vulcanizate characteristics

Glass transition temperature (°C)	Mean molecular weight M (g/mol)	Density	Hardness SHORE A	Poisson's ratio
~ − 70	75000	1.12	48	0.49999

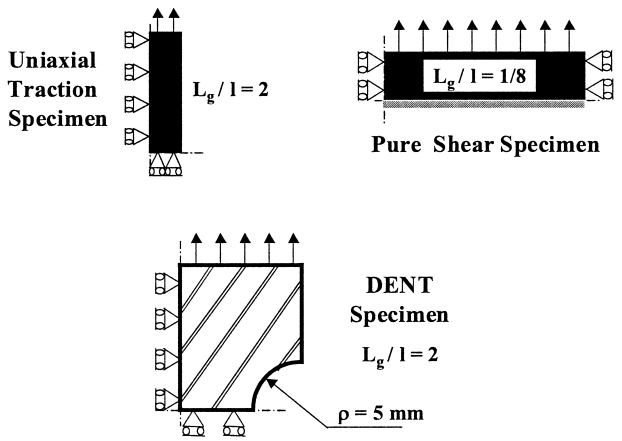

Fig. 1. Sketches of the three tensile tests specimens (L_g: gauge length, l: width of the specimen).

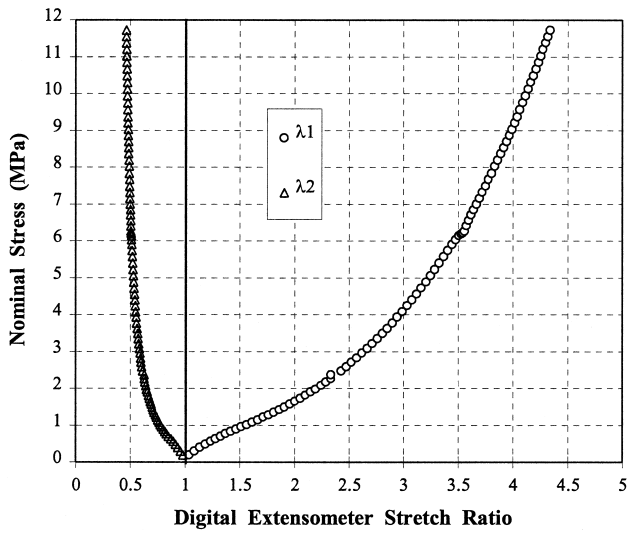

Fig. 2. Two-dimensional experimental data from UT test on non-preconditioned CB filled NR.

area of the camera sensor. The value of each pixel ranges from 0 to 255 with the lowest value corresponding to black, highest value to white, and intermediate values to different shades of gray. These images are stored on a PC hard disk.

A digital image processing, based on correlation calculations, gives access to the two-dimensional displacement components with a subpixel accuracy [1].

3.3. Experimental results for non-preconditioned material

3.3.1. Uniaxial traction tests

Displacement-controlled quasi-static UT tests have been performed on rectangular sheets of non-preconditioned CB filled NR (see Table 3 for the experimental operating conditions). The sketch of the specimen is shown in Fig. 1. Both axial and transverse stretch ratios have been measured using nine digital markers ('virtual extensometers') set out on the sample. Then, the experimental principal axial stretch ratio λ_1 and transverse one λ_2 are given by the mean-value measurements of the reliable extensometers, selected according to the validation criterion based on the allowable amount of shear strain, and previously established by a calibration discussed in Ref. [1]. Fig. 2 shows the evolution of the nominal stress versus the experimental principal stretch ratios λ_1 and λ_2, respectively. The 'nominal stress' (also called First Piola–Kirchhoff stress) refers to the current load F per unit of initial cross-section S_0. One can mention the non-linear behaviour of the material, and the large stretch level achieved (approximately 350% of nominal strain), with a strong strain-stiffening at high stretches, due to a crystallization effect [42]. Furthermore, one can notice the overlapping of some speckle measurement values, due to the sliding of the sample between the pneumatic grips. No additional extension has been measured, which illustrates the suitability of the digital extensometry in case of large strains measurements.

3.3.2. Pure shear tests

Displacement-controlled quasi-static PS tests have been carried out on rectangular sheets of non-preconditioned CB filled NR (see Table 4 for the experimental operating conditions). Fig. 1 displays the sample geometry in case of PS loading conditions. Recall that the lateral displacement is constrained in such a manner that the transverse stretch ratio must remain constant and equal to unity ($\lambda_2 = 1$). Both axial and transverse stretch ratios have been measured using nine digital extensometers set out on the sample, and selected

Table 3
The experimental conditions for the UT tests on non-preconditioned CB filled NR vulcanizate

Light source	Scale factor (μm/pixel)	Correlation size (pixel)	Gauge length L_g (mm)	Strain increment (%)	Strain rate (s^{-1})
Ar + laser	11.7	50	0.702	3.3	0.0024

Table 4
The experimental conditions for the PS tests on non-preconditioned CB filled NR vulcanizate

Light source	Scale factor (μm/pixel)	Correlation size (pixel)	Gauge length L_g (mm)	Strain increment (%)	Strain rate (s^{-1})
Ar + Laser	12.9	50	0.775	1.0	0.0017

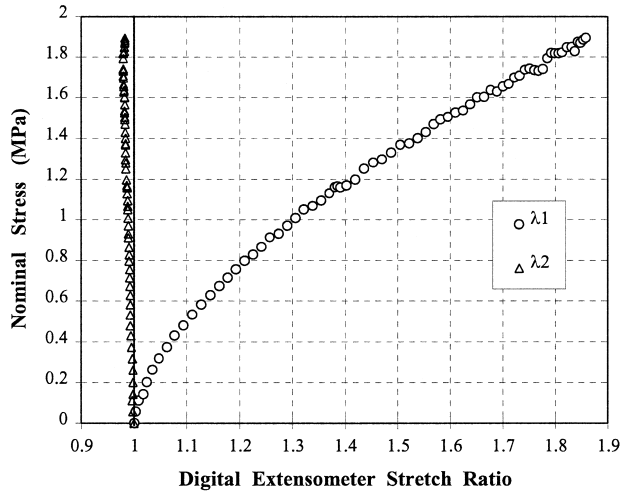

Fig. 3. Two-dimensional experimental data from PS test on non-preconditioned CB filled NR.

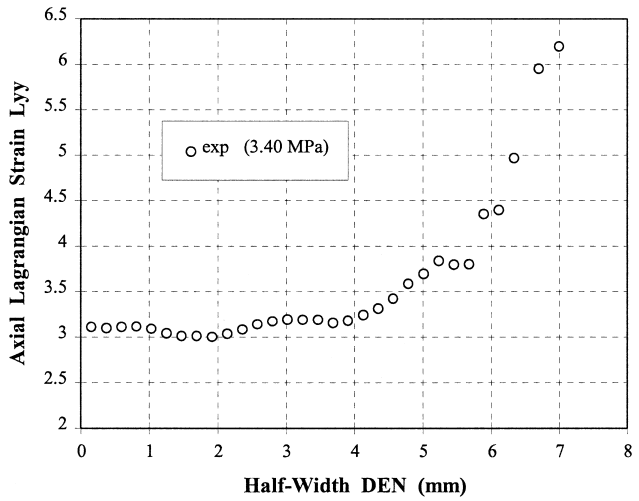

Fig. 4. Experimental axial Lagrangian strain profile measured from a tensile test on a DENT sample (non-preconditioned CB filled NR) (local strain measurement using a digital speckle extensometer).

according to the PS limits test validation criterion ($0.975 \leq \lambda_2 \leq 1$) [1]. The experimental axial and transverse stress-stretch curves are displayed in Fig. 3.

3.3.3. Tensile tests on double-edge notched tensile (DENT) specimens

Displacement-controlled quasi-static tensile tests have been performed on double-edge notched specimens, perforated using a sharp punch (see Fig. 1 for the geometry of the sample and Table 5 for the experimental operating conditions). We have imposed a strain increment of 1.5%,

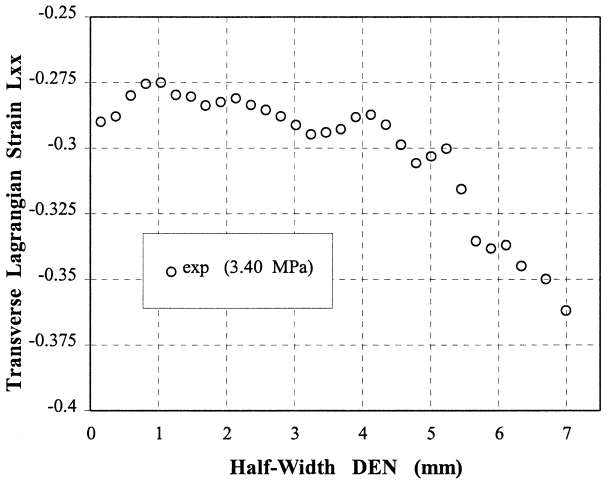

Fig. 5. Experimental transverse Lagrangian strain profile measured from a tensile test on a DENT sample (non-preconditioned CB filled NR) (local strain measurement using a digital speckle extensometer).

seeking for a compromise between the correlation reliability and the local-gradient-strain-measurement sensitivity, especially close to the notches. In practice, local strain measurements have been carried out by setting digital subsets between the notches. Figs. 4 and 5 show the evolution of the axial and the transverse Lagrangian strain profiles along the half-width of a DENT sample, at a given nominal stress. This application illustrates then an interesting feature of the digital extensometry, that is the local strain measurement. In particular, as shown in Section 5, we will use these local strain profiles for the validation of the constitutive law, by comparison with the numerical ones issued from a FEA computation.

3.4. Experimental results for preconditioned material

3.4.1. Cyclic preconditioning procedure

Displacement-controlled quasi-static cyclic tests have been performed on rectangular sheets of CB filled NR. The cyclic loading is under UT or PS conditions, whether the material subsequently undergoes simple tension or PS tests. The loading direction corresponds to the calandering one.

The material is said to be preconditioned if the cyclic loops converge, that is if the rubber approaches a steady state with a constant stress–strain behaviour. In practice, the cyclic preconditioning consists in 10 cycles at 0.01 Hz for a given level of stretch. Fig. 6 shows the cyclic preconditioning of the material under UT loading conditions. Effective stabilization is observed from the fifth cycle. Notice that loading and unloading paths do not rigorously coincide, the

Table 5
The experimental conditions for the tensile tests on DENT samples of non-preconditioned CB filled NR vulcanizate

Light source	Scale factor (μm/pixel)	Correlation size (pixel)	Gauge length L_g (mm)	Strain increment (%)	Strain rate (s^{-1})
Ar + Laser	22.1	50	0.900	1.5	0.0009

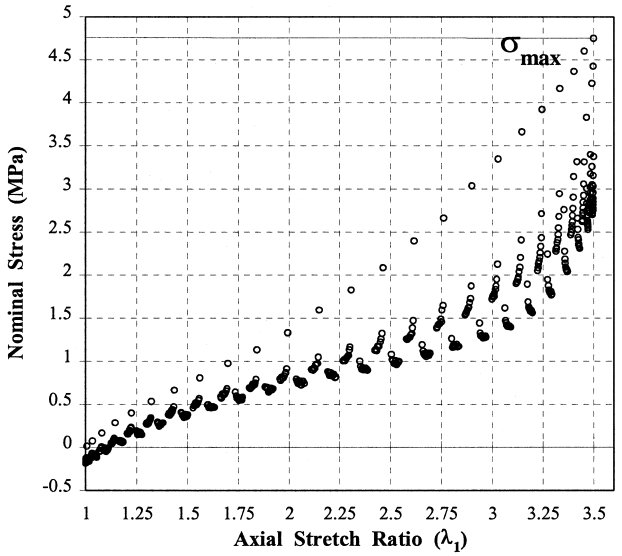

Fig. 6. Preconditioning procedure under UT loading conditions of a CB filled NR vulcanizate sample.

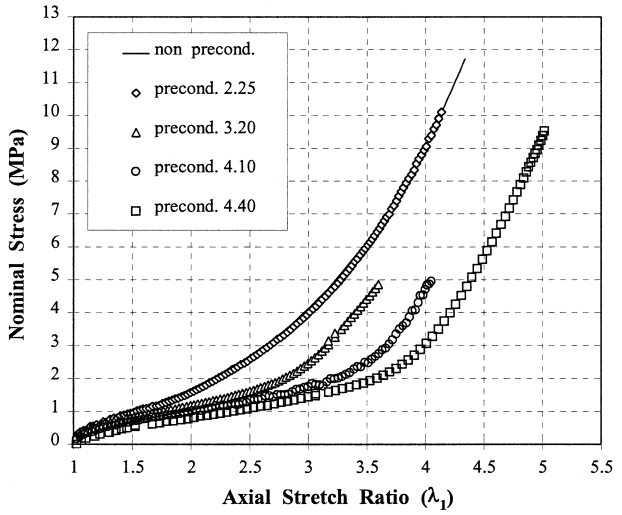

Fig. 7. Stress–strain response of non-preconditioned and preconditioned CB filled NR vulcanizate under UT loading conditions (in terms of axial stretch ratio).

behaviour being rather hysteretic. Furthermore, the material exhibits some permanent set, characterized by a negative load corresponding to the buckling of the specimen at zero displacement. Nevertheless, these departures from a perfectly elastic behaviour are not significant (the dissipated energy remains minor relatively to the strain density energy stored by the material during the deformation), and thus will be neglected.

Because of some expected sliding of the sample between the clamps, the effective preconditioning stretch level is marked as follows: for a given test, the maximum nominal stress, denoted σ_{max} (see Fig. 6), and achieved at the end of the first cyclic loading path is determined. The corresponding axial stretch ratio is then deduced by relating the nominal stress to the corresponding stretch level from the stress–strain curve of the non-preconditioned material, issued from the digital speckle extensometers measurements (Fig. 2 for the simple tension test and Fig. 3 for the PS test). Tables 6 and 7 summarize the operating conditions for the preconditioning procedure in case of simple tension and PS loadings, respectively. One can notice the increasing discrepancy between the imposed and the effective axial stretch ratio, especially at high strain levels. This highlights the relevance of the digital speckle extensometry, especially for large strain measurements.

Table 6
The experimental preconditioning conditions in simple tension loading

Imposed λ_1	Effective λ_1	σ_{max} (MPa)	$\dot{\varepsilon}$ (s^{-1})
2.25	2.25	2.00	0.025
3.50	3.20	4.80	0.050
4.75	4.10	9.80	0.075
5.00	4.40	11.80	0.080

3.4.2. Uniaxial traction tests

Subsequently to the preconditioning, and after a short time rest (approximately 15 mn) to circumvent any self-heating of the sample, displacement-controlled quasi-static simple tension tests have been carried out. The experimental operating conditions are listed in Table 8 (λ_{1P} refers to the axial stretch level preconditioning). As for the non-preconditioned material, the two-dimensional displacement field and thus both the principal axial and transverse stretch ratios have been measured.

Fig. 7 shows the evolution of the stress-stretch experimental curves for both the non-preconditioned and the preconditioned materials at different axial stretch levels λ_{1P}. Three facts are worth mentioning. The first one concerns the non-preconditioned material and the preconditioned one at $\lambda_{1P} = 2.25$. The two curves are superimposed, which indicates that the preconditioning has not induced molecular network rearrangements enough to observe a strong stiffness reduction. This is corroborated by the slight stress-softening preconditioning cycles displayed on Fig. 8. The second fact is relative to the enhancement of the softening and the non-linear behaviour with the stretch level preconditioning. We can finally notice that the prestressed material seems to not recover the behaviour of the non-preconditioned one above the stretch level preconditioning. This is due to the crystallization phenomenon generally encountered for NR vulcanizates, as underlined by Harwood et al. [42], among others.

Fig. 9 shows the evolution of the transverse versus the

Table 7
The experimental preconditioning conditions in PS loading

Imposed λ_1	Effective λ_1	σ_{max} (MPa)	$\dot{\varepsilon}$ (s^{-1})
3.40	3.00	3.25	0.048

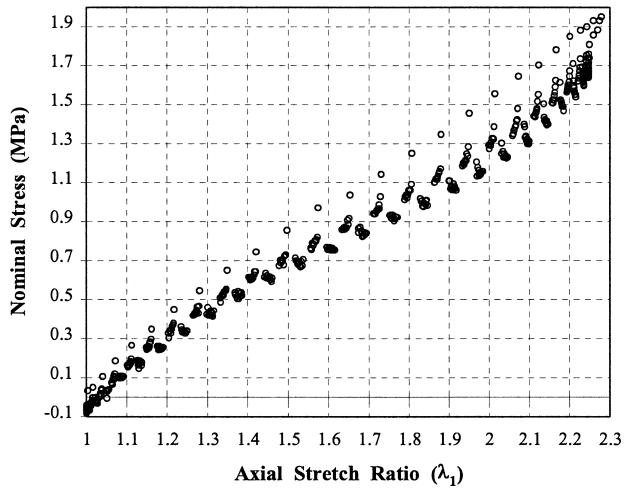

Fig. 8. Preconditioning procedure under UT loading conditions of a CB filled NR vulcanizate sample ($\lambda_{1P} = 2.25$).

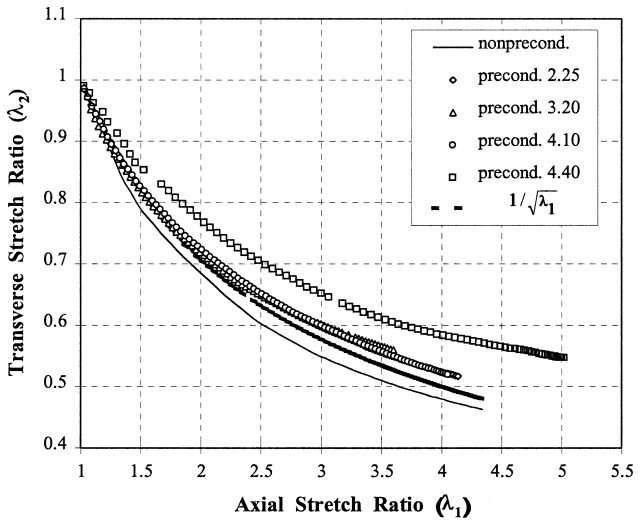

Fig. 9. UT test response of non-preconditioned and preconditioned CB filled NR vulcanizate (in terms of transverse stretch ratio).

axial stretch ratios, for both non-preconditioned and preconditioned materials. We have also plotted the analytical evolution of the transverse stretch ratio for an isotropic and incompressible material loaded in simple tension that is following an inverse square root function of the axial stretch ratio. One can notice the strong shift from this theoretical evolution for the sample which has undergone the largest extension level preconditioning ($\lambda_{1P} = 4.40$).

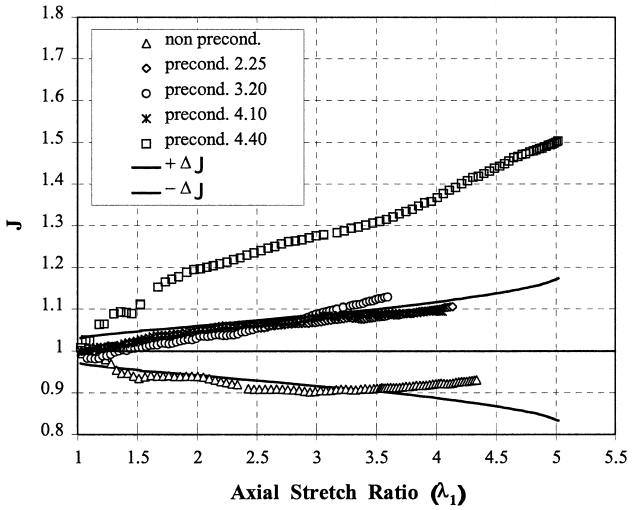

Fig. 10. Volume changes associated with the deformation of non-preconditioned and preconditioned CB filled NR vulcanizate under UT loading conditions (assuming transverse isotropy through the cross-section of the sample).

A more relevant variable can be plotted: the evolution of the total volume change during the deformation process. This variable, denoted J, is defined as:

$$J = \sqrt{I_3} = \lambda_1\lambda_2\lambda_3 \tag{16}$$

or:

$$J = \sqrt{I_3} = \lambda_1\lambda_2^2 \tag{17}$$

if the behaviour is assumed to be isotropic, at least through the cross-section of the material.

Fig. 10 shows the evolution of J for the non-preconditioned and the preconditioned specimens. On the latter graph, $+\Delta J$ and $-\Delta J$ refer to the upper and the lower deviations of J from unity, taking into account the cumulative errors on the experimental stretch ratios measurements (established in Ref. [1]). As already expected from the results of Fig. 9, significant changes of volume are observed for the material preconditioned at $\lambda_{1P} = 4.40$. This might be due to the failure of either the isotropy hypothesis or more probably to the incompressibility one, because of some cavitation in the material.

3.4.3. Pure shear tests

As for the simple tension tests, displacement-controlled quasi-static PS tests have been performed on the preconditioned material, after a short rest time (see Table 9 for the

Table 8
The experimental conditions for the UT tests on preconditioned material

	Light source	Scale factor (μm/pixel)	Correlation size (pixel)	Gauge length L_g (mm)	Strain increment (%)	Strain rate (s^{-1})
$\lambda_{1P} = 2.25$	Ar + laser	12.9	50	0.775	3.1	0.0031
$\lambda_{1P} = 3.20$	Ar + laser	12.9	50	0.775	3.1	0.0031
$\lambda_{1P} = 4.10$	Ar + laser	12.9	50	0.775	3.4	0.0034
$\lambda_{1P} = 4.40$	Ar + laser	12.9	50	0.775	3.2	0.0021

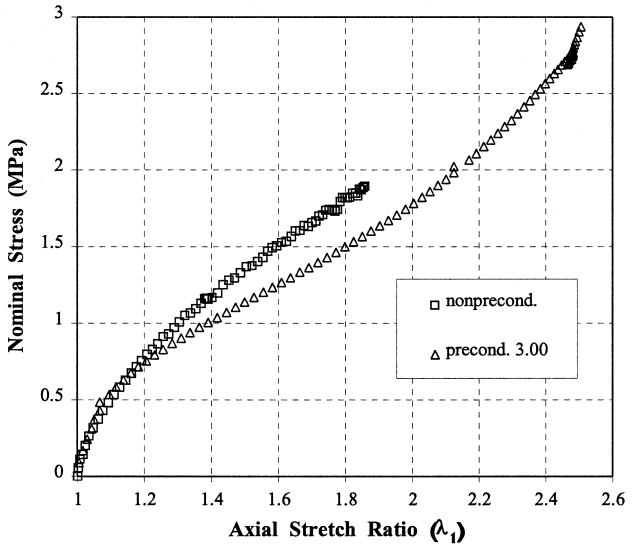

Fig. 11. Stress–strain response of non-preconditioned and preconditioned CB filled NR vulcanizate under PS loading conditions (in terms of axial stretch ratio).

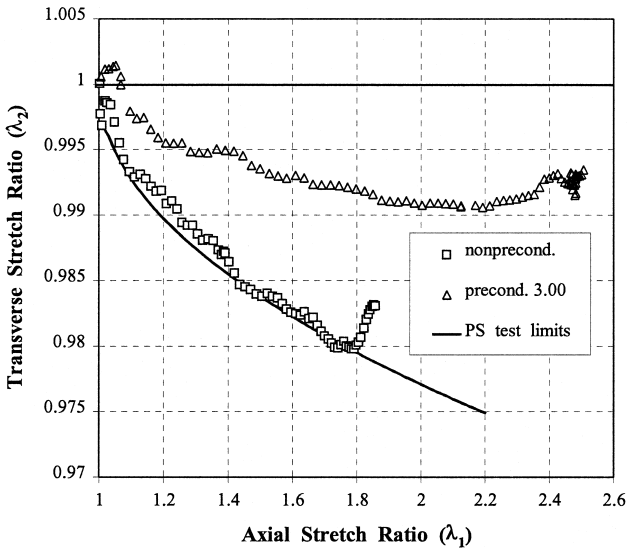

Fig. 12. PS test response of non-preconditioned and preconditioned CB filled NR vulcanizate (in terms of transverse stretch ratio).

experimental operating conditions). Figs. 11 and 12 respectively show the evolution of the nominal stress versus the axial stretch ratio and the transverse one. One can notice that the lateral displacement constraint is satisfied, the transverse stretch ratio λ_2 remaining within the PS test limits (Fig. 12), previously established by a numerical calibration [1]. Furthermore, no significant changes of

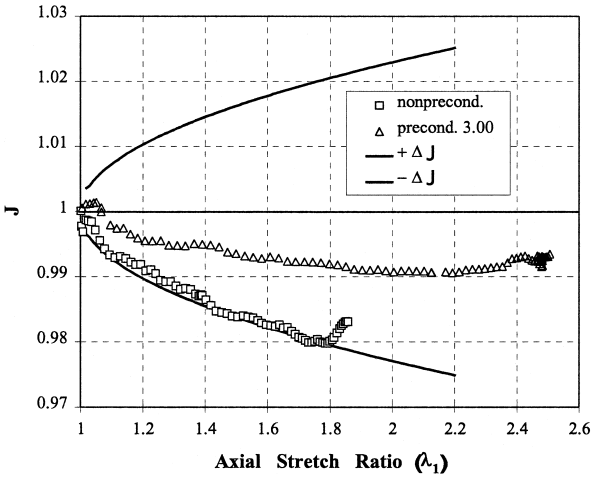

Fig. 13. Volume changes associated with the deformation of non-preconditioned and preconditioned CB filled NR vulcanizate under PS loading conditions (assuming transverse isotropy through the cross-section of the sample).

volume have been observed during the deformation process (Fig. 13).

3.4.4. Some features of the stress-softening effect

The experimental results presented above highlight the hyperlastic behaviour of the material, with a significant part of strain-induced stress-softening effect. One wonders whether this phenomenon is recoverable (time dependent effect?) and if any anisotropy is strain-induced by the preconditioning of the material.

(a) Is there any strain-induced anisotropy? Before seeking for any strain-induced anisotropy, we have performed simple tension tests on the virgin material (non-preconditioned), by cutting off samples along the calandering direction (denoted 'A' for axial direction) and perpendicular to it (denoted 'T' for transversal direction). The operating conditions are given in Table 10. The evolutions of the nominal stress versus the axial and the transverse stretch ratios, respectively, highlight the initial isotropy of the material (Fig. 14).

The next step concerns what we called the 'mixed' tests. The latter consist first in a simple tension preconditioning of the material, cutted off in a direction orthogonal to the calandering one. A new sample is then cutted off from the preconditioned specimen, in such a way that the subsequent UT loading is along the calandering direction (see Fig. 15). We have measured the axial and the transverse stretch ratios, using the experimental conditions listed in Table 11 (λ_{AP} and λ_{TP} denote the axial and the transversal

Table 9
The experimental conditions for the PS tests on preconditioned material

	Light source	Scale factor (μm/pixel)	Correlation size (pixel)	Gauge length L_g (mm)	Strain increment (%)	Strain rate (s^{-1})
$\lambda_{1P} = 3.00$	Ar + laser	13.2	50	0.792	1.0	0.0017

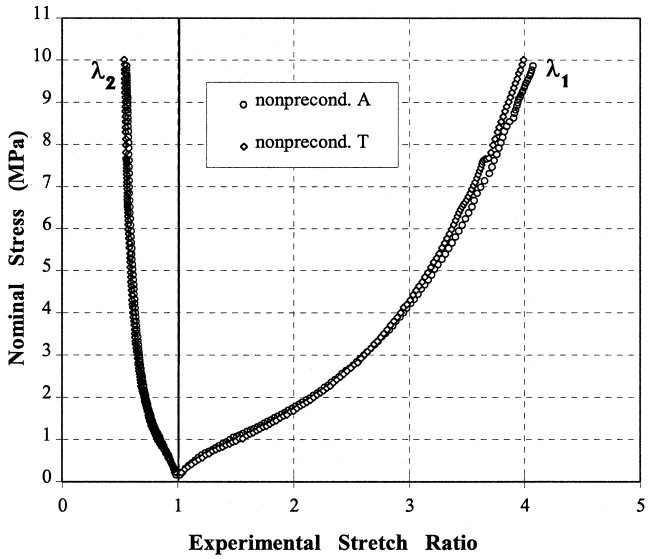

Fig. 14. Experimental data from UT tests on non-preconditioned CB filled NR vulcanizate: an initially isotropic behaviour.

preconditionings, respectively). Fig. 16 shows the experimental stress-stretch curves for the mixed tests. One can notice a lower stiffness reduction for the mixed samples in comparison with the 'axial' ones, even if the preconditioning extension level is higher. These experimental results point out the strain-induced anisotropy due to the preconditioning procedure. Mullins [24] has also mentioned that the degree of softening was not the same in all directions for dumb-bells cut both along and perpendicular to the direction of subsequent stretch, and thus anisotropic stress–strain properties were developed.

(b) Recoverable or Unrecoverable effect? To assess in which extent the stress-softening effect may be considered as permanent, allowing us to model it using a damage approach, we have performed tensile tests on samples previously stretched under UT loading conditions at different axial stretch ratio levels. Then, the specimens have been released and allowed to recover for various periods, at both ambient and elevated temperatures (in

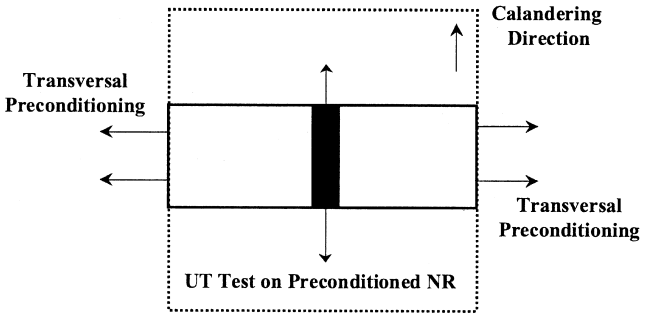

Fig. 15. Samples cutting procedure for the mixed tests.

vacuum (15 mbar) at 95 °C), to know whether the rubber recovers to its initial state, and if so, the rate at which it recovers and the dependence of this rate on conditions such as temperature. If no recovery has taken place at room temperature, even after a long period (approximately 3 months), two days at 95 °C were sufficient for samples to restore their stress–strain properties, the stress-stretch curves of the preconditioned specimens being superimposed to the non-preconditioned material's one (Fig. 17). Qualitative analogous results have been evidenced by Mullins [24] and Rigbi [43], among others.

4. Identification procedure

4.1. The phenomenological constitutive model

Our own interest in elastic behaviour of rubbers falls within the scope of the phenomenological approach. We have adopted a strain invariant based model, especially the so-called third-order deformation approximation for the strain energy density function (Eq. (7)). The latter captures the inextensibility of the network chains, allowing us to account for the strain-stiffening at higher stretches.

Moreover, we are concerned with a continuum formulation of the Mullins effect. According to our experimental observations (progressive and permanent stiffness

Table 10
The experimental conditions for the UT tests on virgin samples cutted off along the calandering direction (axial direction) and orthogonal to it (transversal direction)

	Light source	Scale factor (μm/pixel)	Correlation size (pixel)	Gauge length L_g (mm)	Strain increment (%)	Strain rate (s^{-1})
Axial direction	Ar + laser	22.1	50	1.325	3.1	0.0021
Transversal direction	Ar + laser	22.1	50	1.325	3.1	0.0021

Table 11
The experimental conditions for the UT tests on the mixed samples

	Light source	Scale factor (μm/pixel)	Correlation size (pixel)	Gauge length L_g (mm)	Strain increment (%)	Strain rate (s^{-1})
$\lambda_{AP} = 3.20$	Ar + laser	12.9	50	0.775	3.1	0.0031
$\lambda_{TP} = 3.45$	Ar + laser	10.2	50	0.611	3.3	0.0021

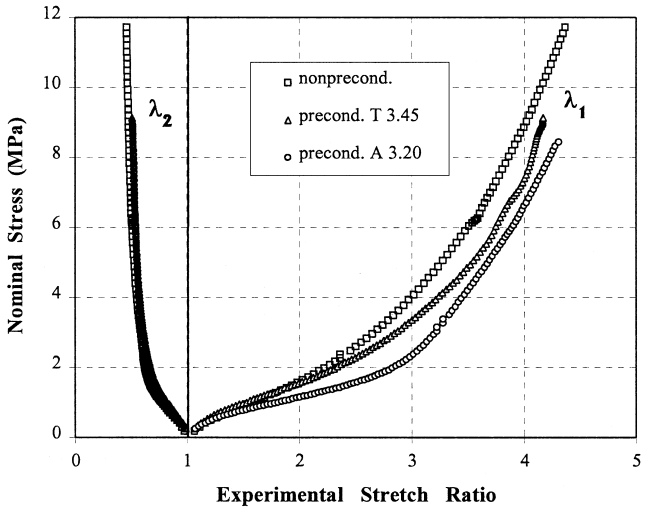

Fig. 16. UT preconditioning tests on CB filled NR vulcanizate: strain-induced anisotropy.

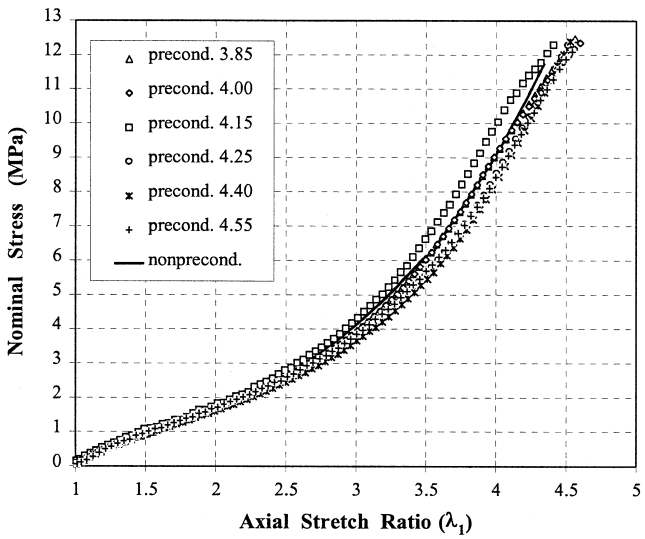

Fig. 17. Recovery of stress-softening after heating in vacuum at 95 °C for 48 h.

reduction), we have used the Miehe's model to account for the discontinuous and continuous damage mechanisms. The constitutive expressions are given by Eqs. (12), (14) and (15). It is assumed throughout that shortcomings like residual strains (also called permanent set) and hysteresis effects are not taken into account. In particular, we idealize the stress response in such a way that the unloading path coincides with the re-loading one, and that no further damage occurs while unloading.

Table 12 summarizes the phenomenological constitutive model. There are nine material parameters to identify: the five c_{ij} parameters of the strain energy density function, and the four damage variables (d_α, η_α) and (d_β, η_β) governing the discontinuous and continuous damage mechanisms of the strain-induced stress-softening effect.

We present hereafter the non-linear optimization procedure for the identification of the constitutive law parameters.

4.2. The constitutive equation parameters identification

There are many ways to fit a theoretical curve to an experimental data. In the present paper, the material constants are numerically determined by means of a least squares non-linear optimization procedure based on the Levenberg–Marquardt–Fletcher (LMF) algorithm [44]. Considering a given deformation state, the parameters identification procedure consists in minimizing a cost function, which expresses the deviation between the experimental stress–strain curve (or load–displacement curve for an inhomogeneous test) and the simulated one. Errors in parameter determination can easily be made if insufficient experimental data is available. Attention must then be paid to the experimental database used for the parameters identification, especially to avoid failures in the numerical simulation of the mechanical response of realistic components under arbitrary multiaxial loading conditions. Tests with a significant deformation mode are for example

Table 12
The strain-induced stress-softening hyperelastic constitutive model

Free energy	$W = (1-d)W_0$
Undamaged free energy	$W_0 = c_{10}(I_1-3) + c_{01}(I_2-3) + c_{11}(I_1-3)(I_2-3) + c_{20}(I_1-3)^2 + c_{30}(I_1-3)^3$
Strain invariants	$I_1 = \lambda_1^2+\lambda_2^2+1/\lambda_1^2\lambda_2^2$, $I_2 = 1/\lambda_1^2+1/\lambda_2^2+\lambda_1^2\lambda_2^2$ (assuming incompressibility)
Damage variable	$d = d_\alpha(\alpha) + d_\beta(\beta)$
Discontinuous damage evolution	$d_\alpha(\alpha) = d_\alpha^\infty\left[1-\exp\left(-\frac{\underset{s\in[0,t]}{\text{Max}}\, W_0(s)}{\eta_\alpha}\right)\right]$
Continuous damage evolution	$d_\beta(\beta) = d_\beta^\infty\left[1-\exp\left(-\frac{\int_0^t \langle \dot{W}_0(s)\rangle \mathrm{d}s}{\eta_\beta}\right)\right]$

the UT test, the equibiaxial test, the planar (or PS) test and the volumetric test.

4.2.1. Expression of the experimental biaxial stresses

The homogeneous tests of our experimental database consist in UT and planar tests. In both cases, the axial and the transverse stretch ratios are measured thanks to the two-dimensional digital speckle extensometer. The dual variables of the principal stretch ratios λ_1 and λ_2, that is the analytical expressions of the nominal stresses or First Piola–Kirchhoff (PK1) stress tensor components, are given by:

$$\sigma_1 = \frac{\partial}{\partial \lambda_1}[(1-d)W_0] \tag{18}$$

$$\sigma_2 = \frac{\partial}{\partial \lambda_2}[(1-d)W_0]$$

For the UT tests, the experimental data is thus:

$$\sigma_1^{\mathrm{UT}} \equiv \sigma_{1\,\mathrm{exp}}^{\mathrm{UT}} = \left(\frac{F}{S_0}\right)_{\mathrm{UT}}$$

and

$$\sigma_2^{\mathrm{UT}} \equiv \sigma_{2\,\mathrm{exp}}^{\mathrm{UT}} = 0 \text{ by definition} \tag{19}$$

where F refers to the current load and S_0 is the initial cross-section of the specimen. As for the PS or planar data, it is given by:

$$\sigma_1^{\mathrm{PS}} \equiv \sigma_{1\,\mathrm{exp}}^{\mathrm{PS}} = \left(\frac{F}{S_0}\right)_{\mathrm{PS}} \tag{20}$$

4.2.2. Position of the optimization problem

Consider $(\lambda_{1n}, \lambda_{2n}, (\sigma_{1\,\mathrm{exp}})_n, (\sigma_{2\,\mathrm{exp}})_n)$, $1 \le n \le N$, N quadruplets of experimental data corresponding to the experimental principal stretch ratios and the dual nominal stresses, respectively, for both UT and PS tests (N is given by the product of the number of tests by the number of points per curve). Consider too the N couples $(\sigma_{1n}, \sigma_{2n})$ of principal First Piola–Kirchhoff stresses obtained by Rivlin's model and corresponding to stretches $(\lambda_{1n}, \lambda_{2n})$. We introduce the residue vector $(2N \times 1)$ defined by:

$$R = (R_1, R_2)^{\mathrm{t}} \tag{21}$$

where R_1 and R_2 are two tables $(N \times 1)$ whose components are:

$$(R_l)_n = (\sigma_l)_n - (\sigma_{l\,\mathrm{exp}})_n \qquad l = 1,2 \;\; 1 \le n \le N \tag{22}$$

Our constitutive model constants are ranked in the following vector (dimension $(1 \times M)$, $1 \le M \le 9$):

$$X = (\alpha_1, \ldots, \alpha_M)^{\mathrm{t}} \tag{23}$$

where the nine constants α_i are namely:

$$\begin{aligned} &\alpha_1 = c_{10}, \quad \alpha_2 = c_{01}, \quad \alpha_3 = c_{11}, \quad \alpha_4 = c_{20}, \\ &\alpha_5 = c_{30}, \quad \alpha_6 = d_\alpha^\infty, \quad \alpha_7 = \eta_\alpha, \quad \alpha_8 = d_\beta^\infty, \\ &\alpha_9 = \eta_\beta \end{aligned} \tag{24}$$

We aim to minimize with respect to X, the cost function f defined by:

$$f(X) = \sum_{l=1}^{2} \sum_{n=1}^{N} (R_l)_n^2 = R^{\mathrm{t}} R \tag{25}$$

To solve this problem, we use an iterative algorithm in which first and second derivatives of the function f are evaluated. The latter are given, respectively, by:

$$J(X) \equiv \left[\frac{\partial f}{\partial X_i}\right]_i = 2 \cdot A \cdot R \tag{26}$$

and:

$$H(X) \equiv \left[\frac{\partial^2 f}{\partial X_i \, \partial X_j}\right]_{i,j} = 2 \cdot A \cdot A^{\mathrm{t}} + 2\left[R_i \cdot \frac{\partial^2 R_i}{\partial X_j \, \partial X_k}\right]_{j,k} \tag{27}$$

where A is the transposed Jacobian matrix of dimension $(2N \times M)$ defined by:

$$A_{ij} = \frac{\partial R_j}{\partial X_i} \qquad 1 \le i \le 2M \;\; 1 \le j \le 2N \tag{28}$$

Finally, since the components $R_i(X)$ of residue vector R are 'very small' when one gets close enough to the solution, the second derivative or Hessian $H(X)$ given by Eq. (27) can be approximated by the expression:

$$H(X) \approx 2 \cdot A \cdot A^{\mathrm{t}} \tag{29}$$

Notice that the expressions of the cost function gradient J and the Hessian H are written in an analytical form, issued from the differentiation of the cost function with respect to each component of the parameters vector X previously defined. This allows us to avoid any inaccurate evaluation of the gradient, which is a step of prime importance in an optimization procedure. The research of the minimum of the cost function is achieved using the LMF algorithm (see Appendix A).

4.3. Results and discussion

We present here the results relative to the identification of the constitutive law parameters, for both the UT and the PS tests, and taking into account the stress-softening effect.

Table 13 lists the numerical values of the nine parameters of our constitutive model. Fig. 18 provides a comparison between the experimental data corresponding to the UT preconditioning of the material at a given stretch ratio level ($\lambda_{1\mathrm{P}} = 3.20$), and the numerical results given by the identified model. Only the loading paths of the first, second, fifth and tenth cycles have been plotted. One can notice that

Table 13
Numerical values of the identified constitutive model parameters

c_{10} (MPa)	c_{01} (MPa)	c_{11} (MPa)	c_{20} (MPa)	c_{30} (MPa)	d_α^∞	η_α (MPa)	d_β^∞	η_β (MPa)
0.567	−0.078	−0.0008	0.0006	0.0013	0.741	17.3	0.228	22.3

the predicted curves agree well with the experimental ones. Thus, taking into account the strain-history deformation, this model gives an accurate response of the material, both under UT loading conditions at increasing preconditioning extension levels (Figs. 19 and 20), and for biaxial tests like the PS one, as depicted in Fig. 21.

5. Numerical simulation

This section intends to show original results, relative to the validation of the identified constitutive model using local strain measurements performed on a non-preconditioned DENT specimen (see geometry on Fig. 1) under tensile loading conditions. First, we give some computational aspects of the implementation of the Rivlin's constitutive law into the finite element code SYSTUS [45]. For the sake of simplicity, we neglected here the damage occurring during the mechanical loading of the non-preconditioned material. So, the implemented model did not incorporate the strain-induced stress-softening effect. Nevertheless, details of such a numerical implementation are given in Miehe [41]. We end this section with a comparison between our experimental data and the numerical results issued from a FEA computation.

5.1. Finite element implementation

5.1.1. Rubber elasticity and finite element analysis

Traditionally, rubber elasticity problems involve large strains, non-linear hyperelasticity and no change (or very little change) of volume upon deformation. Thus, rubber is also classified as incompressible or nearly-incompressible material. Furthermore, the analysis of elastomeric components response is often represented in numerical modelling as isotropic and hyperelastic, in spite of some shortcomings like strain-rate dependence, energy dissipation, Mullins effect, different stiffness under static or dynamic loads and so on.

Other than the difficulties associated with the solution of non-linear problems resulting from constitutive and geometric non-linearities, a tricky task consists in the proper treatment of incompressibility. Indeed, in FEA, the requirement of incompressibility condition imposes a severe constraint to the Galerkin equations, inducing locking to the finite element model and ill-conditioning of the stiffness matrix, for example.

Since the incompressibility constraint results directly from the volumetric strain (or its stress counterpart, the hydrostatic pressure), the strain density energy function is usually splitted into two distinct parts: isochoric due to distortion and dilatation due to volume change. These two

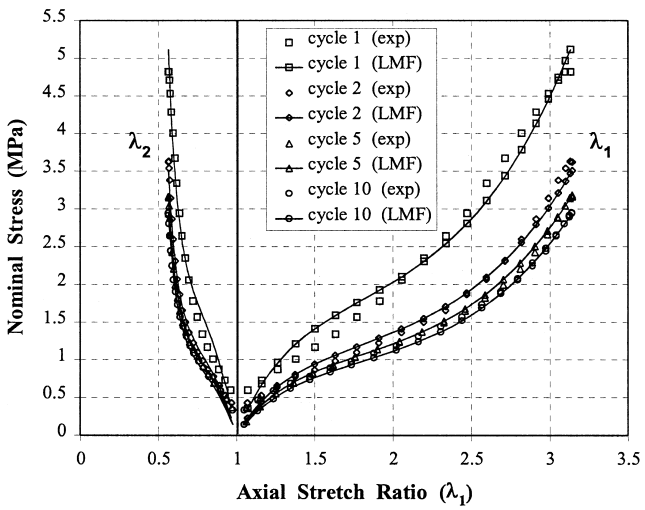

Fig. 18. Prediction of the evolution of the stress response of the NR vulcanizate while preconditioning, using our strain-induced softening hyperelastic model (in terms of the axial stretch ratio λ_1 and the transverse stretch ratio λ_2).

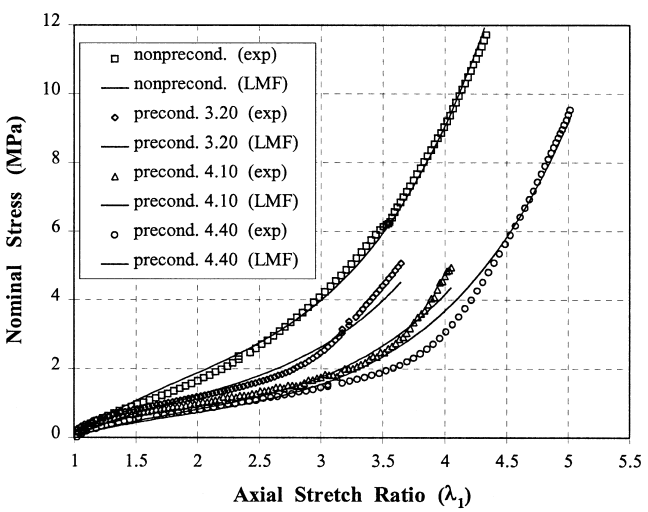

Fig. 19. Prediction of the stress response of the NR vulcanizate preconditioned at increasing extension levels under UT loading conditions, using our strain-induced softening hyperelastic model (in terms of the axial stretch ratio λ_1).

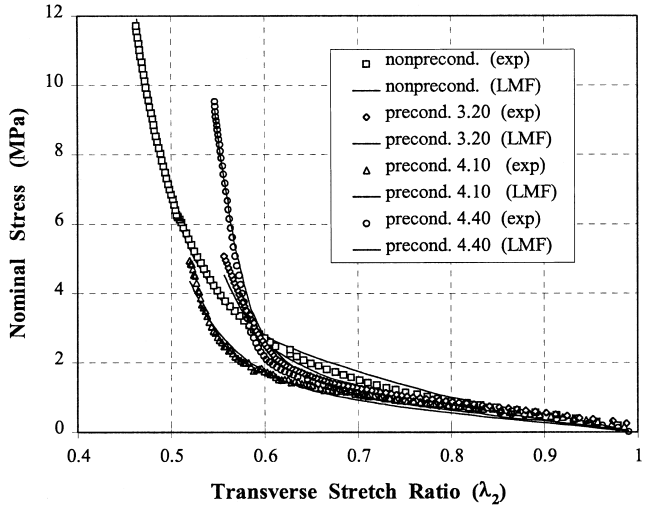

Fig. 20. Prediction of the stress response of the NR vulcanizate preconditioned at increasing extension levels under UT loading conditions, using our strain-induced softening hyperelastic model (in terms of the transverse stretch ratio λ_2).

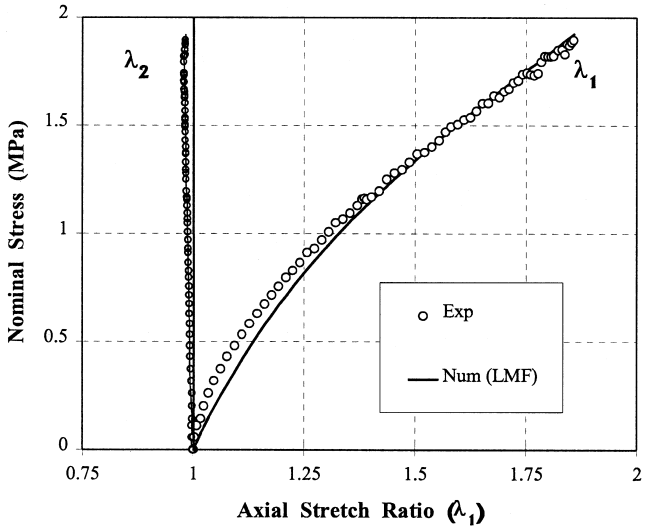

Fig. 21. Prediction of the stress response of the non-preconditioned NR vulcanizate under PS loading conditions, using our strain-induced softening hyperelastic model (in terms of the axial stretch ratio λ_1 and the transverse stretch ratio λ_2).

parts can of course be interpolated differently in finite element approximations, using appropriate shape functions.

Two approaches are commonly used in dealing with incompressibility. The first one is the so-called mixed formulation (see for instance Refs. [46,47] among others). In this approach, a Lagrange multiplier field (hydrostatic pressure p) is used to impose the incompressible condition, but in this case, for each time step, the unknown value p is to be computed (in addition to stress and strain) at the level of element.

We preferred the second method, that is the penalty formulation, to implement the 3-D, plane strain and plane stress formulations for the Rivlin's model in the SYSTUS FEA code. The penalty method has encountered a great success in the treatment of the incompressibility constraint, and it is usually applied in conjunction with reduced integration technique [48,49]. Furthermore, we adopted the Total Lagrangian formulation, that is the geometric setting relative to the initial configuration, to ensure material frame invariance. This requires that the constitutive model is formulated in terms of the Green–Lagrange strain (or Right Cauchy–Green dilatation) and the second Piola–Kirchhoff stress.

5.1.2. Basic equations

By assuming that the material is homogeneous, incompressible and isotropic in the undeformed state, the isothermal hyperelastic constitutive law is derived from a strain energy density function per unit volume written in terms of the strain invariants I_1, I_2 and I_3 previously defined. According to the split hypothesis of the strain energy density function into dilatational and deviatoric components, one can write the following expression:

$$W''(I_1, I_2, I_3) = W(I_1, I_2) + K(I_3) \tag{30}$$

where the isochoric term $W(I_1, I_2)$ is approximated with the Rivlin's law given in Eq. (7), and $K(I_3)$ is the bulk energy. The latter may be written in terms of a penalty function $G(I_3)$ and a penalty factor κ as follows:

$$K(I_3) = \frac{1}{2}\kappa[G(I_3)]^2 \tag{31}$$

Liu [50] has analysed several expressions for the penalty function. Two formulations are commonly used. The first one is proposed by Oden [51]:

$$G(I_3) = \frac{1}{2}(I_3 - 1) \tag{32}$$

and the second one follows from the work by Häggbland and Sundberg [47]:

$$G(I_3) = \frac{1}{2}\ln(I_3) \tag{33}$$

where 'ln' denotes the Napierian logarithm function. In this work, we used the latter expression, the first one violating the continuum mechanical principle that the energy should be infinite when the volume is reduced to zero.

The penalty factor κ is more or less equivalent to the elastic bulk modulus. Its expression is generally connected to the Poisson's ratio ν and determined from the boundary conditions. For the Rivlin's model we used the same expression as in [52]:

$$\kappa = (c_{10} + c_{01})\frac{6(1-\nu)}{(1+\nu)(1-2\nu)} - 4(c_{10} + 2c_{01}) \tag{34}$$

Notice that because of a mathematically undefined term in Eq. (34), only nearly-incompressible material can be evaluated. Nevertheless, the values of Poisson's ratio over 0.499 are mostly sufficient to describe incompressible behaviour.

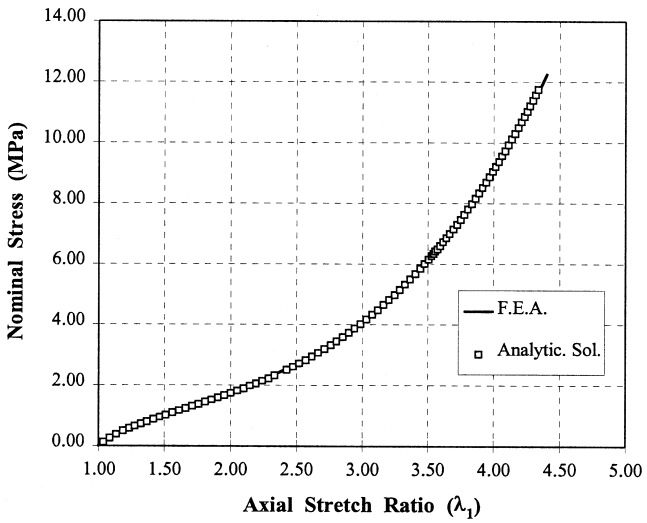

Fig. 22. Validation of the implementation procedure by comparison between the FEA and the analytical solution in UT loading condition.

Before deriving the constitutive tensors, remember that in the general case of the three-dimensional state, the strain invariants are explicitly written in terms of the Right Cauchy–Green dilatation components C_{ij} as follows:

$$\begin{aligned} I_1 &= C_{11} + C_{22} + C_{33} \\ I_2 &= C_{11}C_{22} + C_{11}C_{33} + C_{22}C_{33} - C_{12}^2 - C_{13}^2 - C_{23}^2 \\ I_3 &= C_{11}C_{22}C_{33} - C_{11}C_{23}^2 - C_{22}C_{13}^2 - C_{33}C_{12}^2 \\ &\quad + 2C_{12}C_{23}C_{13} \end{aligned} \tag{35}$$

The second Piola–Kirchhoff stress tensor $\bar{S}$ is formed according to the following formula:

$$S_{ij} = \frac{\partial W(I_1, I_2)}{\partial L_{ij}} + \kappa G(I_3)\frac{\partial G(I_3)}{\partial L_{ij}} \tag{36}$$

where L_{ij} are the Green–Lagrange strain tensor components. Using the relation between the Right Cauchy–Green dilatation tensor and the Green–Lagrange strain tensor given by ($\bar{I}$ denotes the identity matrix):

$$\bar{L} = \frac{1}{2}(\bar{C} - \bar{I}) \tag{37}$$

one may write:

$$\begin{cases} S_{ij} = 2\dfrac{\partial W}{\partial I_1}\dfrac{\partial I_1}{\partial C_{ij}} + 2\dfrac{\partial W}{\partial I_2}\dfrac{\partial I_2}{\partial C_{ij}} + 2\kappa G(I_3)\dfrac{\partial G}{\partial I_3}\dfrac{\partial I_3}{\partial C_{ij}} & \text{if } i = j \\ S_{ij} = \dfrac{\partial W}{\partial I_1}\dfrac{\partial I_1}{\partial C_{ij}} + \dfrac{\partial W}{\partial I_2}\dfrac{\partial I_2}{\partial C_{ij}} + \kappa G(I_3)\dfrac{\partial G}{\partial I_3}\dfrac{\partial I_3}{\partial C_{ij}} & \text{if } i \neq j \end{cases} \tag{38}$$

It should be noted that the term κG in the latter equations had to be adjusted by a hydrostatic pression p_0, to ensure zero stresses condition in the undeformed configuration.

These conditions are namely:

$$\begin{cases} S_{ij} = 0 \\ C_{ij} = \delta_{ij} \end{cases} \tag{39}$$

i.e $I_1 - 3 = I_2 - 3 = 0$, which gives the following expression for the hydrostatic pressure p_0:

$$p_0 = -2c_{10} - 4c_{01} \tag{40}$$

and finally leads to the constitutive equations:

$$\begin{cases} S_{ij} = 2\dfrac{\partial W}{\partial I_1}\dfrac{\partial I_1}{\partial C_{ij}} + 2\dfrac{\partial W}{\partial I_2}\dfrac{\partial I_2}{\partial C_{ij}} + 2X\dfrac{\partial I_3}{\partial C_{ij}} & \text{if } i = j \\ S_{ij} = \dfrac{\partial W}{\partial I_1}\dfrac{\partial I_1}{\partial C_{ij}} + \dfrac{\partial W}{\partial I_2}\dfrac{\partial I_2}{\partial C_{ij}} + X\dfrac{\partial I_3}{\partial C_{ij}} & \text{if } i \neq j \\ \text{with } X = \dfrac{1}{2I_3}[\kappa G(I_3) + p_0] \end{cases} \tag{41}$$

By a further derivation, the material constitutive tensor $\bar{\bar{D}}$ can be obtained, the terms of which are:

$$D_{ijkl} = \frac{\partial S_{ij}}{\partial L_{kl}} \tag{42}$$

These terms are computed in accordance with the symmetry of the stress and the strain tensors, that is:

$$D_{ijkl} = D_{jikl} = D_{ijlk} = D_{klij} \tag{43}$$

which corresponds to the evaluation of 21 components:

$$[D]_{ijkl} = \begin{bmatrix} D_{1111} & D_{1122} & D_{1133} & D_{1123} & D_{1131} & D_{1112} \\ & D_{2222} & D_{2233} & D_{2223} & D_{2231} & D_{2212} \\ & & D_{3333} & D_{3323} & D_{3331} & D_{3312} \\ & & & D_{2323} & D_{2331} & D_{2312} \\ & SYM & & & D_{3131} & D_{3112} \\ & & & & & D_{1212} \end{bmatrix} \tag{44}$$

Finally, the 2-D plane strain and plane stress are two particular cases of the 3-D one. Indeed, the plane strain state leads to the following simplification:

$$\begin{cases} C_{13} = C_{23} = 0 \\ C_{33} = 1 \end{cases} \tag{45}$$

As for the plane stress state, one may write, assuming incompressibility:

$$\begin{cases} S_{13} = S_{23} = S_{33} = 0 \\ I_3 = 1 \Rightarrow C_{33} = \dfrac{1}{C_{11}C_{22} - C_{12}^2} \end{cases} \tag{46}$$

Before ending this section, we have performed some numerical tests to check the right implementation of our model into the finite element code. The results of such analysis have been compared to those issued from analytical solutions in case of UT (Fig. 22) and PS (Fig. 23) loading

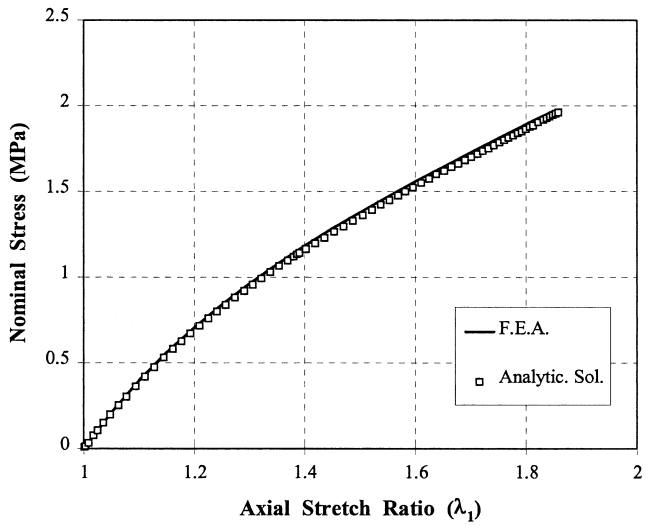

Fig. 23. Validation of the implementation procedure by comparison between the FEA and the analytical solution in PS loading condition.

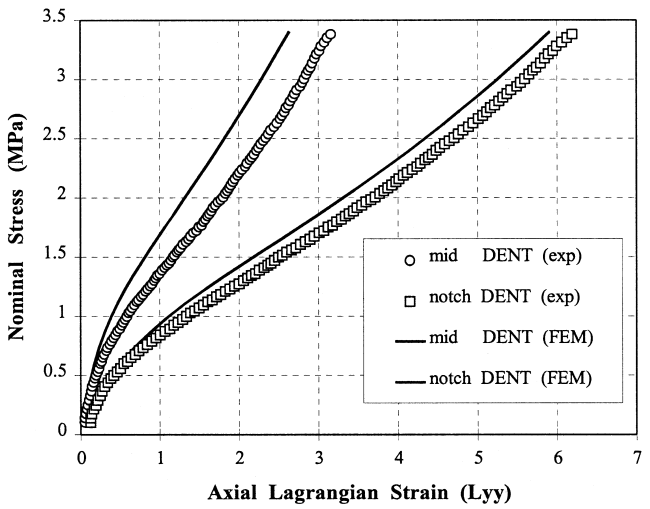

Fig. 25. Validation of the constitutive model for the non-preconditioned material: comparison between experimental and numerical stress-stretch curves at the mid and notch zones of the DENT specimen.

conditions, and found to be in a very good agreement, which validated the implementation procedure.

5.2. Results and discussion

The validation methodology proposed here involves the local strain measurements allowed by our two-dimensional non-contact extensometer, and performed on a non-preconditioned DENT sample. The constitutive law parameters have been re-identified, neglecting the stress-softening effect occurring while loading the specimen. These constants were calculated from UT and PS experimental data for the non-preconditioned material ($c_{10} = 0.310$ MPa, $c_{01} = 0.255$ MPa, $c_{11} = -0.033$ MPa, $c_{20} = 0.034$ MPa and $c_{30} = 0.0003$ MPa). Hence, no inverse method, based on a FEA of a structural component has been used for their evaluation.

According to symmetry considerations, only the quarter of the DENT sample has been meshed using 162 eight-node quadratic elements (see Fig. 24). Furthermore, the boundary conditions are also depicted in Fig. 24, the applied loading consisting in the vertical displacement of the upper part of the specimen.

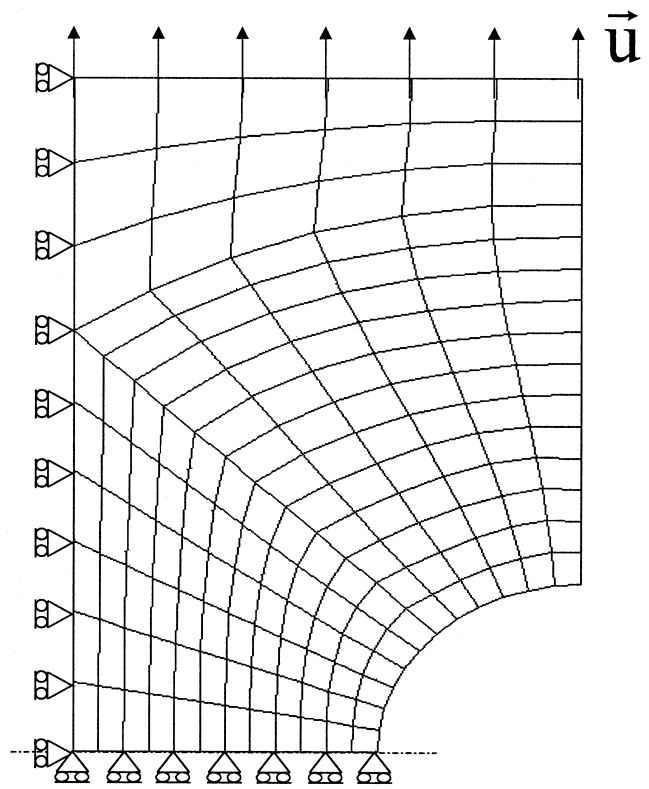

Fig. 24. Mesh of the DENT sample (162 eight-node quadratic elements).

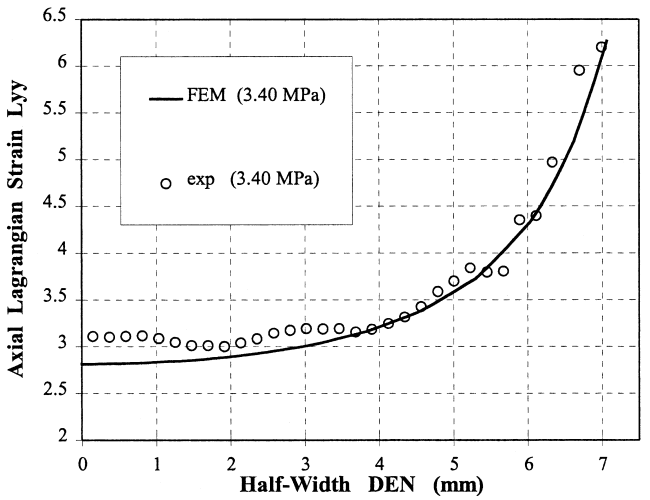

Fig. 26. Validation of the constitutive model for the non-preconditioned material: comparison between experimental and numerical axial strain profiles along the half-width of the DENT sample.

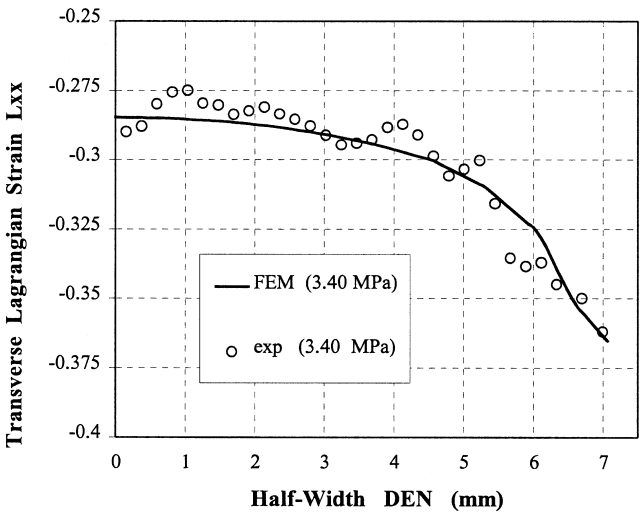

Fig. 27. Validation of the constitutive model for the non-preconditioned material: comparison between experimental and numerical transverse strain profiles along the half-width of the DENT sample.

The numerical results of the F.E. analysis are displayed in Figs. 25–27, along with the experimental data. The results consist in the stress–strain curves measured in the mid zone and at notch region of the specimen for the first comparison, and the evolution of the axial and the transverse Lagrangian strain profiles along the half-width of the sample. In all cases, one can observe the good agreement between the experimental and the numerical results, especially the right prediction of the stress level in the specimen. We can also notice the right evaluation of the strain gradient along the half-width of the specimen, the gap between experimental and numerical results not exceeding 7% close to the notch, and approximately 15% in the mid zone of the specimen, because of the wave-like aspect of the experimental profiles, probably due to a sliding of the sample between the clamps. Indeed, the digital extensometry provide a reliable tool for the characterization of the mechanical behaviour of elastomers, and thus for the modelling of their constitutive equations.

6. Concluding remarks and discussion of future work

In this paper, we have developed a relevant methodology for the mechanical behaviour characterization of a CB filled NR vulcanizate by means of a non-contact two-dimensional speckle extensometer. More generally, the present development is suitable for a structural analysis of rubber components under biaxial loadings.

Through the experimental part of this work, we have established the suitability of the digital extensometry in case of large strains measurements. Furthermore, we have pointed out the interest of two-dimensional in-plane displacement field measurements, especially to check some hypothesis like incompressibility and its evolution while loading the specimen, generally admitted for such materials. Finally, we have presented an interesting feature of the two-dimensional extensometry, that is the local strain measurements performed on structural components.

As for the numerical part, by developing the basic formulas, we have shown how it is possible to solve an optimization problem and to increase the robustness and the efficiency of the non-linear optimization procedure when using experimental biaxial data. Then, we have derived the basic formulas to implement any hyperelastic model, written in terms of a strain energy density function, in the finite element formulation. Finally, we have proposed an original way to validate a constitutive model, by a FEA performed on a structural component, for which the measurement of local strains has been found to be in good agreement with the numerical predictions.

Concerning the constitutive equation, we have shown how it is possible to take into account the Mullins' effect using Miehe's model, and how to couple it to the hyperelastic Rivlin's model in order to phenomenologically describe the mechanical behaviour of the CB filled NR vulcanizate.

In a future work, the identification of more realistic models for rubbery components needs to circumvent some shortcomings like permanent set or hysteresis dissipative loops. This may be achieved by using the superimposed finite elastic–viscoelastic–plastoelastic-with-damage model proposed by Miehe and Keck [53], or the pseudo-elastic model by Ogden and Roxburgh [54]. Furthermore, the current models allow the stiffness reduction description occurring while loading the material. Nevertheless, the damage-induced compressibility may also be taken into account, by a proper modification of both the isochoric and the volumic parts of the strain energy density function.

From the experimental standpoint, the identification of reliable constitutive equations is not a trivial task, and is of course dependant on the experimental data available. Thus, the two-dimensional strain measurements provide a powerful tool to increase the efficiency of the optimization procedures. More generally, within the trend of the inverse methods, and using the strain fields experimentally measured, the constraint of performing homogeneous tests no longer exists, and it is then possible to identify material parameters from non-homogeneous multiaxial tests. Moreover, realistic boundary conditions may thus be determined and imposed when performing FEA, which ensures realistic and reliable results issued from numerical computations.

Acknowledgements

The authors are indebted to Paulstra Hutchinson (France) for supplying the material.

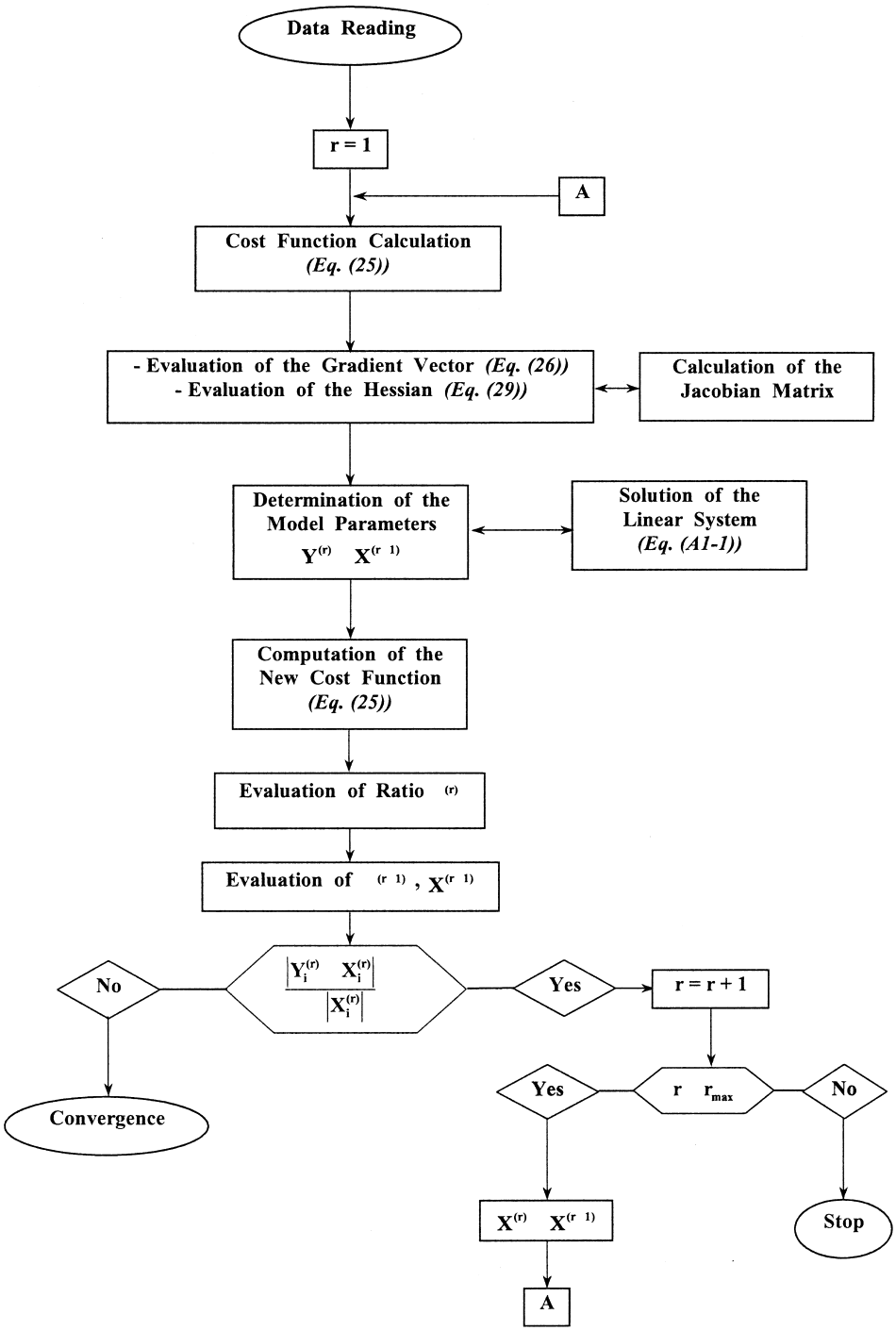

Fig. A1. LMF optimisation procedure flowchart.

Appendix A. The Levenberg–Marquardt–Fletcher's algorithm

The research of the minimum of the cost function is achieved using an iterative method consisting in generating an approximation sequence $X^{(r)}$ given by:

$$X^{(r+1)} = X^{(r)} + \delta^{(r)} \tag{A1}$$

where, for each iteration, we solve a problem of the following type:

$$\text{Find } \delta^{(r)} \text{solution of Inf}\{q^{(r)}(\delta), \|\delta\| \leq h^{(r)}\} \tag{A2}$$

where $q^{(r)}(\delta)$ is a quadratic approximation of $f(X^{(r)} + \delta)$, obtained from a truncated Taylor series expansion about X,

and defined by:

$$q^{(r)}(\delta) = f(X^{(r)}) + J^{(r)t}\delta + \frac{1}{2}\delta^{t}H^{(r)}\delta \tag{A3}$$

$J^{(r)} = J(X^{(r)})$ given by Eq. (26), $H^{(r)} = H(X^{(r)})$ given by Eq. (29) and $h^{(r)} \geq 0$ is a parameter to be defined.

An analysis of the problem [44] shows that if $\delta(r)$ is a solution of the problem and if $\|\cdot\|$ is an euclidian norm, there exists $\nu^{(r)}$ such that:

$$(H^{(r)} + \nu^{(r)}I)\delta^{(r)} = -J^{(r)} \tag{A4}$$

where I is the unit $(M \times M)$ matrix and $\nu^{(r)}$ a positive real. According to Fletcher [44], the parameter $\nu^{(r)}$ is actualized following a rule which takes into account the 'quality' of approximation of the function f by the quadratic form $q^{(r)}$ by means of a coefficient $\rho^{(r)}$ given by:

$$\rho^{(r)} = \frac{\Delta f^{(r)}}{\Delta q^{(r)}} \tag{A5}$$

where:

$$\Delta f^{(r)} = f(X^{(r)}) - f(X^{(r)} + \delta^{(r)}) \tag{A6}$$

and:

$$\Delta q^{(r)} = f(X^{(r)}) - q^{(r)}(\delta^{(r)}) \tag{A7}$$

So, the approximation of f by $q^{(r)}$ to iteration r is much accurate as the coefficient $\rho^{(r)}$ is closer to the unit. The optimization procedure flowchart is summarized in Fig. A1. In practice, two additional parameters have been introduced: the τ constant, which allows one to avoid any numerical indeterminations when $X^{(r)}$ is almost zero, and the ε parameter, which is the stopping criterion in case of convergence.

References

[1] Laraba-Abbès F, Ienny P, Piques R. Submitted for publication.
[2] Wall FT. J Chem Phys 1942;10:132.
[3] Flory PJ, Rehner Jr. J. J Chem Phys 1943;11:512.
[4] Treloar LRG. Rep Progr Phys 1943;9:113.
[5] James HM, Guth E. Phys Rev 1941;59:111.
[6] James HM, Guth E. J Chem Phys 1947;15:669.
[7] Wang MC, Guth E. J Chem Phys 1952;20:1144.
[8] Arruda EM, Boyce MC. J Mech Phys Solids 1993;41(2):389.
[9] Rivlin RS. Rubber Chem Technol 1992;65:G51.
[10] Charlton DJ, Yang J. Rubber Chem Technol 1994;67(3):481.
[11] Mooney M. J Appl Phys 1940;11:582.
[12] Tschoegl NW. J Polym Sci 1971;A1(9):1959.
[13] James AG, Green A, Simpson GM. J Appl Polym Sci 1975;19:2033.
[14] Morman KN, Pan TY. Rubber Chem Technol 1988;61:503.
[15] Ogden RW. Proc R Soc Lond 1972;A326:565.
[16] Hill R. J Mech Phys Solids 1968;16:229.
[17] Hill R. Proc R Soc Lond A 1970;314:457.
[18] Bouasse H, Carriere Z. Annal de la Faculté des Sci Toulouse 1903;5:257.
[19] Schwartz AJ. Inst Elec Engng 1910;44:693.
[20] Beadle C, Stevens HP. J Chem Soc 1911;30:1421.
[21] Gurney HP, Travener CH. Ind Engng Chem 1922;14:134.
[22] Somerville AA, Cope WH. Trans Iri 1928;4:263.
[23] Holt WL. Rubber Chem Technol 1932;5:79.
[24] Mullins L. J Rubb Res 1947;16(12):275.
[25] Mullins L. J Phys Coll Chem 1950;54:239.
[26] Bueche F. J Appl Polym Sci 1960;4(10):107.
[27] Dannenberg EM. Trans Iri 1966;42:26.
[28] Boonstra BB. In: Kraus G, editor. Reinforcement of elastomers. Interscience; 1965.
[29] Mullins L, Tobin NR. Rubber Chem Technol 1957;30:551.
[30] Bueche F. J Appl Polym Sci 1961;5:271.
[31] Harwood JAC, Mullins L, Payne AR. J Appl Polym Sci 1965;9:3011.
[32] Harwood JAC, Payne AR. J Appl Polym Sci 1966;10:315.
[33] Harwood JAC, Payne AR. J Appl Polym Sci 1966;10:1203.
[34] Johnson MA, Beatty MF. Continuum Mech Thermodyn 1993;5:301.
[35] Johnson MA, Beatty MF. Int J Engng Sci 1995;2:223.
[36] Govindjee S, Simo J. J Mech Phys Solids 1991;39(1):87.
[37] Lemaître J. Nuclear Engng Des 1984;80:233.
[38] Kachanov LM. Introduction to continuous damage mechanics. Dordrecht: Martinus Nijhoff Publishers; 1986.
[39] Chaboche JL. J Appl Mech 1988;55:59.
[40] Govindjee S, Simo J. J Mech Phys Solids 1992;40(1):213.
[41] Miehe C. Eur J Mech A/Solids 1995;14(5):697.
[42] Harwood JAC, Mullins L, Payne AR. J Iri 1967;17.
[43] Rigbi Z. Adv Polym Sci 1980;36:21.
[44] Fletcher R. Practical methods of optimization. New York: Wiley; 1987.
[45] SYSTUS, FRAMASOFT CSI + Finite Element Code (Release 233).
[46] Malkus DS, Hughes TJR. Comput Meth Appl Engng 1978;15:63.
[47] Häggbland B, Sundberg JA. Comput Struct 1983;17:835.
[48] Malkus DS. Int J Numer Meth. Engng 1980;16:121.
[49] Hughes TJR. The Finite element method. New Jersey: Prentice Hall Publishers; 1987.
[50] Liu C. Traction of automobile tires on snow, an investigation by means of the finite element Method. PhD Thesis at Technical University of Vienna, Austria; 1994.
[51] Oden JT. Finite elements of nonlinear continua. New York: McGraw-Hill; 1972.
[52] Peeken H, Doepper R, Orschall B. Comp. Struct. 1987;26:181.
[53] Miehe C, Keck J. J Mech Phys Solids 2000;48:323.
[54] Ogden RW, Roxburgh DG. Proc R Soc Lond A 1999;(455):2861.